

JGR Space Physics

RESEARCH ARTICLE

10.1029/2021JA029939

Key Points:

- The energetic electrons at the dipolarization fronts (DFs) experience a two-step acceleration process at the reconnection x-line and DFs
- Pancake, Rolling pin, and Cigar distributions are formed in sequence during the propagation of the DFs
- These distributions are resulted from the different time scales of betatron and Fermi mechanisms at the DFs

Correspondence to:

Q. Lu,
qmlu@ustc.edu.cn

Citation:

Huang, K., Lu, Q., Lu, S., Wang, R., & Wang, S. (2021). Formation of Pancake, Rolling-pin, and Cigar distributions of energetic electrons at the dipolarization fronts (DFs) driven by magnetic reconnection: A two-dimensional particle-in-cell simulation. *Journal of Geophysical Research: Space Physics*, 126, e2021JA029939. <https://doi.org/10.1029/2021JA029939>

Received 4 SEP 2021
Accepted 11 OCT 2021

Formation of Pancake, Rolling Pin, and Cigar Distributions of Energetic Electrons at the Dipolarization Fronts (DFs) Driven by Magnetic Reconnection: A Two-Dimensional Particle-In-Cell Simulation

Kai Huang^{1,2} , Quanming Lu^{1,2} , San Lu^{1,2} , Rongsheng Wang^{1,2} , and Shui Wang^{1,2}

¹Department of Geophysics and Planetary Science, CAS Key Lab of Geospace Environment, University of Science and Technology of China, Hefei, People's Republic of China, ²CAS Center for Excellence in Comparative Planetology, Hefei, People's Republic of China

Abstract A two-dimensional particle-in-cell (PIC) simulation is performed to study the formation of the pitch angle distribution of energetic electrons at dipolarization fronts (DFs) driven by magnetic reconnection. The energetic electrons at DFs are originated from the lobe region, and experience a two-step acceleration process at the reconnection x-line and the DFs, respectively. Three kinds of pitch angle distributions commonly observed in the magnetotail, Pancake, Rolling pin, and Cigar distributions, are formed in sequence during the propagation of the DFs. In the early stage, Pancake distributions are formed through betatron acceleration. During this stage, the flux of energetic electrons with pitch angles around 0° and 180° is low because these electrons have no time to be reflected many times at the DFs to obtain sufficient Fermi acceleration. However, the electrons with pitch angles around 90° are difficult to be trapped around the DFs for a long time, and their flux saturates quickly; while the electrons with pitch angles around 0° and 180° can be trapped inside the closed field lines and they get continuous Fermi acceleration during the propagation of the DFs. Therefore, in the later stage, the flux of energetic electrons with pitch angles around 0° and 180° gradually increases and at last exceeds that of energetic electrons with pitch angles around 90°, forming Rolling pin and Cigar distributions in sequence.

Plain Language Summary Energetic electrons in the magnetotail usually show anisotropic pitch angle distributions, such as Pancake, Cigar, and Rolling-pin distributions. All of the three kinds of pitch angle distributions are frequently observed to be related to dipolarization fronts. Pancake distribution is characterized by the enhancement of energetic electron flux with pitch angles around 90°; Cigar distribution is characterized by the enhancement of energetic electron flux with pitch angles around 0° and 180°; Rolling-pin distribution is characterized by the enhancement of energetic electron flux with pitch angles around 0°, 90°, and 180°. It has been long accepted that electrons with pitch angles around 90° are generated by betatron acceleration, and electrons with pitch angles around 0° and 180° are generated by Fermi acceleration. However, the differences in the conditions to form the three kinds of distributions are far less understood. In this paper, we study when and where these distributions can be formed, and the detailed acceleration processes that lead the energetic electrons to form these distributions.

1. Introduction

Dipolarization fronts (DFs), characterized by a sudden increase in the GSM-z component of magnetic field, are frequently observed Earthward propagating structures in the magnetotail (H. Fu et al., 2019; S. Lu et al., 2015; Nakamura et al., 2002; Ohtani et al., 2004; Runov et al., 2009). They are usually accompanied with bursty bulk flows (BBFs) of plasma (Angelopoulos et al., 1992, 1994; Cao et al., 2006). DFs play an important role in the mass and energy transport processes in the magnetosphere (Nakamura et al., 2009, 2011; Volwerk et al., 2008). It is believed to be a generator for the auroral field-aligned currents during substorms (Birn & Hesse, 2013; Borovsky et al., 2019) as well as the generation of nonthermal electrons and ions (Birn et al., 2004; Deng et al., 2010; S. Lu et al., 2016; M. Wu et al., 2015; Zhou et al., 2010).

Energetic electrons at the DFs usually display anisotropic distributions. There are two kinds of typical distributions: Pancake distributions, where the pitch angles of energetic electrons are around 90°, and Cigar

distributions, where the pitch angles of energetic electrons are around 0° and 180° . It has been long accepted that energetic electrons with Pancake distributions are generated by betatron acceleration, where the electron perpendicular energy increases due to the enhancement of the magnetic field while the magnetic moment is kept as a constant (H. S. Fu et al., 2011; C. Huang et al., 2015; P. Wu et al., 2006), and energetic electrons with Cigar distributions are generated by Fermi acceleration (Drake et al., 2006; X. R. Fu et al., 2006; Li et al., 2017; Q. Lu et al., 2018), where the electron parallel energy increases through multiple reflections by the DFs while electrons bounce between the two mirror points close to the Earth along the closed field line. During the bouncing process, the secondary adiabatic invariant $\oint p_{\parallel} ds$ is conserved; therefore, the increase in the parallel energy is related to the shrink of the closed field lines. Recently, a new distribution named Rolling-pin distribution, where the pitch angles of energetic electrons are around 0° , 90° , and 180° , has been observed and is argued to be generated due to the combination of betatron and Fermi accelerations (Liu et al., 2017).

H. S. Fu et al. (2011, 2012) suggested that Pancake distribution is related to DFs associated with growing flux pileup region (FPR, the region with strong magnetic field behind DFs) where the magnetic field increases (Khotyaintsev et al., 2011; Zhang et al., 2007), while Cigar distribution is related to DFs associated with decaying FPR where the magnetic field decreases. They argue that Cigar distribution in a decaying FPR is formed due to the decrease of energetic electron flux with pitch angles around 90° , which is caused by a betatron cooling process because of the attenuation of magnetic field. Through a statistical study of 133 DF events, M. Y. Wu et al. (2013) found that Pancake distribution is dominant in the middle tail, while the occurrence rates of Pancake and Cigar distributions are comparable in the near-Earth region. The reason is attributed to the higher speed flow leading to stronger compression of the magnetic field and thus stronger betatron acceleration in the middle tail. All the above studies attribute the formation of different pitch angle distributions at the DFs to different dominating acceleration mechanisms. However, the energy gain of energetic electrons is not only related to the acceleration power, but also related to the acceleration time. Therefore, the idea in previous studies needs to be revisited and a study of the whole acceleration processes of the energetic electrons at DFs is necessary.

It is generally believed that DFs can be produced by magnetic reconnection (Runov et al., 2012; Sitnov et al., 2009, 2013). In this paper, we perform a two-dimensional (2D) particle-in-cell (PIC) simulation to study the formation of anisotropic pitch angle distribution of energetic electrons at the DFs, which are driven by magnetic reconnection. In the simulation, we can not only calculate the power of different acceleration mechanisms, but also trace the particles to study the detailed acceleration processes and their source regions. We find that different pitch angle distributions of energetic electrons at DFs are formed at different stages of the acceleration process. This result is contrary to previous ideas that different pitch angle distributions are related to different dominating acceleration mechanisms.

2. Simulation Model

A 2D PIC model that solves the electromagnetic field and particle motion self-consistently is employed in this paper. The code has been successfully employed to study magnetic reconnection and plasma waves (Chang et al., 2021; C. Huang et al., 2010; K. Huang et al., 2020; Q. Lu et al., 2010). The simulation is performed on the $x-z$ plane. The initial configuration is a Harris sheet with magnetic field $\mathbf{B}(z) = B_0 \tanh(z/\delta) \mathbf{e}_x$ and plasma density $n(z) = n_0 \operatorname{sech}^2(z/\delta) + n_b$, where B_0 is the asymptotic magnetic field, δ is the half-thickness of the current sheet, n_0 is the peak density of the current sheet, and $n_b = 0.05n_0$ is the background density. The initial distributions of ions and electrons are Maxwellian, while the current sheet populations have drift velocities along the y direction $-V_{i0}/V_{e0} = T_{i0}/T_{e0} = 5$ to satisfy the Ampere's law $\nabla \times \mathbf{B} = \mu_0 \mathbf{J}$. Ion to electron mass ratio is assumed to be $m_i/m_e = 100$. The light speed $c = 15V_A$, where V_A is the Alfvén speed defined by $V_A = B_0/\sqrt{\mu_0 m_i n_0}$. The simulation domain size is $L_x \times L_z = 80d_i \times 40d_i$ with a spatial resolution $\Delta x = \Delta z = 0.05d_i$, where d_i is the ion inertia length based on n_0 . The time step is $\Delta t = 0.001\Omega_i^{-1}$, where $\Omega_i = eB_0/m_i$ is the ion gyrofrequency. Over 2×10^8 particles for each species are used in our simulation. We use magnetic reconnection to drive DFs; therefore, we will not focus on the onset phase of reconnection, and a perturbation on the initial magnetic flux $\Delta\Psi = \Psi_0 \operatorname{sech}^2(x/4\delta) \operatorname{sech}^2(z/\delta)$ is introduced to trigger the reconnection (here $\Psi_0 = 0.05B_0 d_i$, magnetic flux function Ψ satisfies $B_x = \partial\Psi/\partial z$ and $B_z = -\partial\Psi/\partial x$). In the

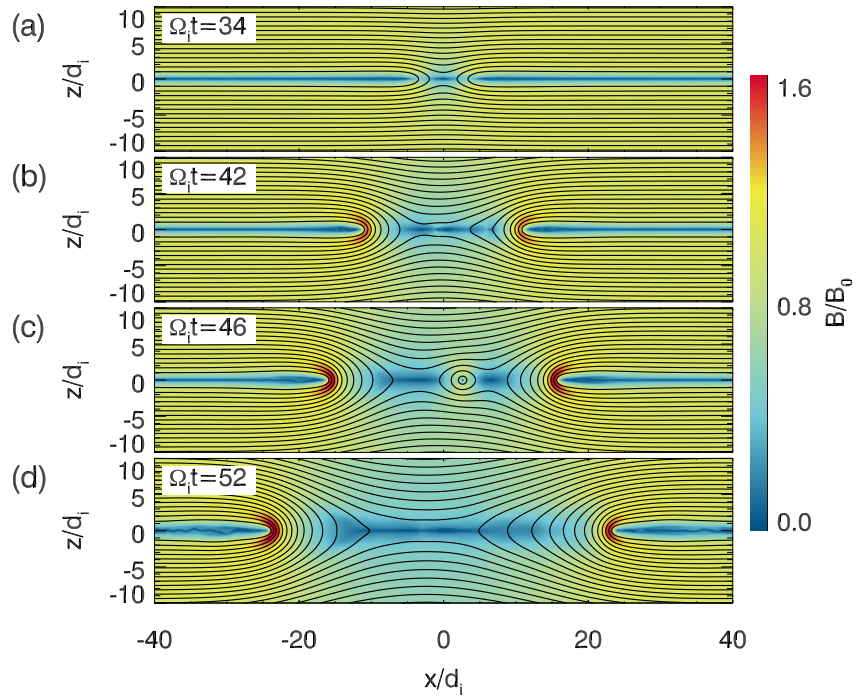


Figure 1. The strength of the total magnetic field B/B_0 at $\Omega_i t = 34, 42, 46,$ and $52,$ respectively. Black curves represent the in-plane magnetic field lines.

x direction, we use periodic boundary conditions, while in the z direction, conducting boundary conditions are used for electromagnetic field and reflecting boundary conditions are used for particles.

3. Simulation Results

3.1. Evolution of the DFs Driven by Reconnection

Figure 1 illustrates the formation process of DFs driven by magnetic reconnection. Panels (a–d) show the time evolution of the magnetic field B/B_0 . The in-plane magnetic field lines are also plotted. At around $\Omega_i t = 34,$

a reconnection x line is formed at $x \approx 0,$ where the magnetic flux is converted from the reconnection in-flow region to the outflow region. Initially, the outflow magnetic field B_z is weak. With the proceeding of reconnection, the amplitude of B_z increases due to the flux pileup by the high-speed electron outflow jets (C. Huang et al., 2015), forming the FPR. Finally, DFs with a peak B_z propagating to the downstream directions are formed. At around $\Omega_i t = 46,$ a secondary magnetic island is generated around $x = 3d_i.$ This magnetic island changes the structure of magnetic field along the x direction. Finally, this magnetic island merges with the FPR behind the DF on the right side.

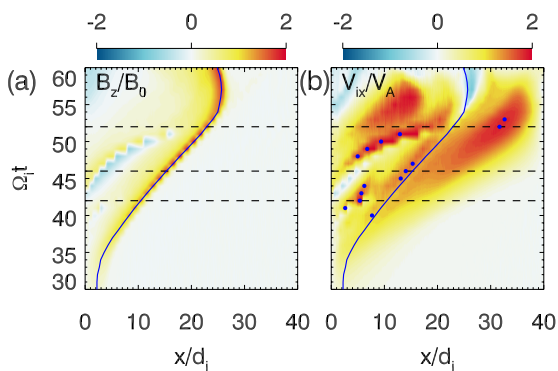


Figure 2. Time stacks of (a) the magnetic field B_z/B_0 and (b) the ion bulk velocity V_{ix}/V_A along $z = 0$ from $\Omega_i t = 30$ to $60.$ Blue curves trace the peak of B_z at each time point, while blue dots represent the peaks of $V_{ix}.$ The three horizontal dashed lines label $\Omega_i t = 42, 46,$ and $52,$ respectively.

Figure 2 shows the time evolution of the magnetic field B_z/B_0 and the ion bulk velocity V_{ix}/V_A along $z = 0.$ Here, only the DF on the right side in Figure 1 is shown. The region with negative B_z corresponding to the secondary magnetic island is shown in Figure 1c. The blue curves trace the time evolution of the peak $B_z,$ while the blue dots denote the peaks of V_{ix} from $\Omega_i t = 40$ to $53.$ Due to the formation of magnetic island behind the DF, the relative position between the peaks of B_z and V_{ix} is complicated: Sometimes the peak of B_z is in front of that of $V_{ix},$ sometimes the peak of B_z is behind that of $V_{ix},$ and sometimes the two peaks are collocated. After

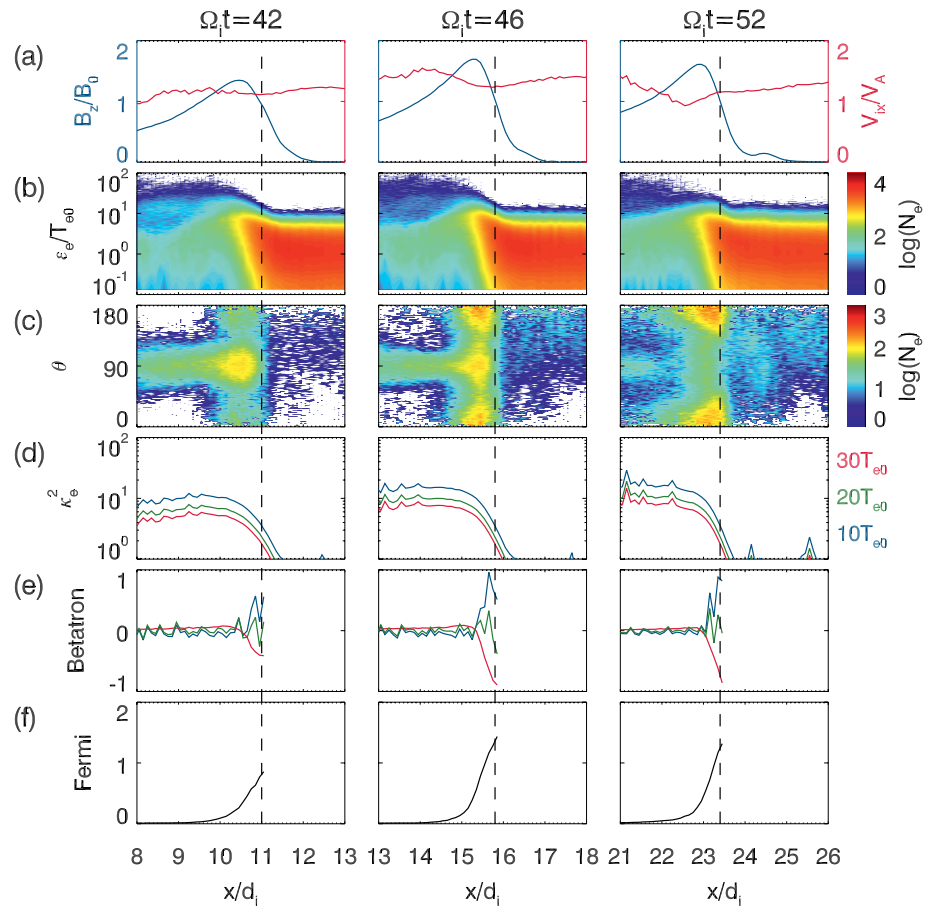


Figure 3. The distributions of some quantities around the DFs at $\Omega_i t = 42, 46,$ and $52,$ respectively. (a) The magnetic field B_z/B_0 and the ion bulk velocity V_{ix}/V_A along $z = 0.$ (b) Electron energy spectra. (c) The pitch angle distributions for electrons with energy larger than $\sim 10T_{e0}.$ (d) Adiabatic parameter κ_e^2 for electrons with perpendicular energy equal to $10, 20,$ and $30T_{e0}.$ (e) Power for betatron acceleration. (f) Power for Fermi acceleration. Vertical black dashed lines separate the region where the adiabatic assumption is valid.

about $\Omega_i t = 55,$ the DF is blocked due to the periodic boundary conditions; we will not focus on this period in this paper. From $\Omega_i t = 40$ to $55,$ the DF propagates along the x direction with a nearly constant speed about $1.25 V_A.$

3.2. Formation of Pancake, Rolling-Pin, and Cigar Distributions at the DFs

The DFs propagates with an almost constant speed from $\Omega_i t = 40$ to $55.$ Then, we will study the detailed characteristics of the energetic electrons at the DFs at $\Omega_i t = 42, 46,$ and 52 (labeled by horizontal dashed lines in Figure 2). The results at the three moments are shown in the left, central, and right columns in Figure 3. Panel (a) shows the magnetic field B_z and x -directional ion bulk velocity $V_{ix}.$ The DFs propagate to the right direction and the FPRs are located on the left side of the DFs. Panel (b) shows the electron energy distributions, and it is clear that electrons are greatly energized in the region at and behind the DFs. At the DFs, the maximum energy of energetic electrons can reach $\sim 30T_{e0}.$ Panel (c) shows the pitch angle distributions of electrons with energy larger than $\sim 10T_{e0}.$ At $\Omega_i t = 42, 46,$ and $52,$ the electron pitch angle distributions show Pancake, Rolling pin, and Cigar signatures, respectively. The magnetic field and flow structures near the DFs at the three moments are similar; however, the pitch angle distributions of energetic electrons are totally different. To find out the reason for this difference, we study the electron energization property near the DFs at the three moments. Using the adiabatic approximation, we calculate the power of betatron and Fermi acceleration based on Equation 1. Here, U_e is the total kinetic energy of electrons, u_E is the $\mathbf{E} \times \mathbf{B}$ drift velocity, and $\kappa = \mathbf{b} \cdot \nabla \mathbf{b}$ is the curvature of the magnetic field. The three terms on the right

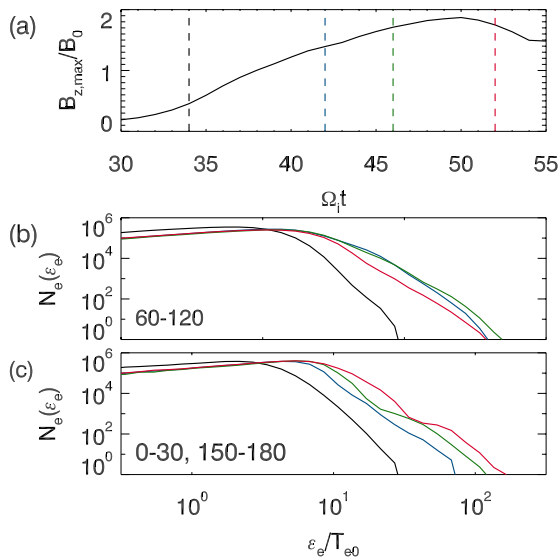


Figure 4. (a) The time evolution of the peak B_z around the DFs from $\Omega_i t = 30$ to 60; black, blue, green, and red dashed lines denote the moment when the energetic electrons satisfy isotropic, Pancake, Rolling pin, and Cigar distributions at the DFs, respectively. (b) The energy spectra for electrons with pitch angle between 60° and 120° at the DFs at $\Omega_i t = 34$ (black), 42 (blue), 46 (green), and 52 (red), respectively. (c) The energy spectra for electrons with pitch angle less than 30° and larger than 150° at the DFs at $\Omega_i t = 34$ (black), 42 (blue), 46 (green), and 52 (red), respectively.

side of Equation 1 represent the power of the acceleration from parallel electric fields, betatron acceleration, and Fermi acceleration, respectively (Dahlin et al., 2014; Northrop, 1963; Wang et al., 2016).

$$\frac{dU_e}{dt} = E_{\parallel} J_{\parallel} + \frac{P_{e\perp}}{B} \left(\frac{\partial B}{\partial t} + \mathbf{u}_E \cdot \nabla B \right) + \left(P_{e\parallel} + m_e n V_z^e \right) \mathbf{u}_E \cdot \boldsymbol{\kappa} \quad (1)$$

This theory is valid when the ratio between the curvature radius of the magnetic field lines and the gyroradius of electrons $\kappa_e^2 = \left(|\boldsymbol{\kappa}| r_e \right)^{-1}$ is larger than 1 (Buchner & Zelenyi, 1989). In panel (d), we plot κ_e^2 for electrons with perpendicular energy equal to 10, 20, and 30 T_{e0} , respectively. We find that in the regions with obvious anisotropic energetic electrons (on the left of the vertical dashed lines), κ_e^2 is larger than one, indicating the feasibility to use Equation 1. In panels (e and f), we plot the power of betatron acceleration and Fermi acceleration averaged between $-0.25d_i < z < 0.25d_i$, which are believed to be the mechanisms to produce energetic electrons with pitch angles around 90° and $0^\circ/180^\circ$. In panel (e), the blue, red, and green lines represent the time partial derivative term $P_{e\perp} \partial B / (B \partial t)$, the gradient drift term $P_{e\perp} \mathbf{u}_E \cdot \nabla B / B$ term, and the sum of these two terms, respectively. Surprisingly, although the pitch angle distributions of energetic electrons are greatly different, the distributions of the power of betatron and Fermi acceleration are similar at the three moments. The power of Fermi acceleration is much larger than that of betatron acceleration. For betatron acceleration, the gradient drift term and the time partial derivative term almost cancel each other. This result indicates that the different pitch angle distributions of energetic electrons cannot be explained by the acceleration mechanism that has the largest power where they are observed.

Figure 3 reveals that the formation of Pancake, Rolling pin, and Cigar distributions is not determined by the dominant acceleration mechanism where the distribution is observed. It implies that these different distributions may be related to electrons with different acceleration process. In Figure 4a, we plot the time evolution of the peak value of B_z at the DFs, and in panels (b and c), we show the energy spectra for electrons with pitch angles around 90° and $0^\circ/180^\circ$, respectively. The black, blue, green, and red curves represent spectra at $\Omega_i t = 34, 42, 46,$ and 52 , respectively, as labeled by the vertical dashed lines in panel (a). The spectra are calculated by the electrons in a square with side length equal to $1.0 d_i$ around the DFs. At $\Omega_i t = 34$, the electron distribution is nearly isotropic. During the propagation of DFs, the peak of B_z at the DFs increases. In the early stage (around $\Omega_i t = 42$), the flux of energetic electrons with pitch angles around 90° is greatly enhanced, and is larger than that of energetic electrons with pitch angles around 0° and 180° . These electrons are accelerated through betatron acceleration due to the increase of B_z . During this stage, the flux of energetic electrons with pitch angles around 0° and 180° is low because these electrons have no time to be reflected many times to get Fermi acceleration. Therefore, a Pancake distribution is formed. In the later stage, at $\Omega_i t = 46$, the peak of B_z is still increasing; however, the flux of energetic electrons with pitch angles around 90° does not change too much and it even decreases at $\Omega_i t = 52$. The reason is that energetic electrons with pitch angle around 90° are not able to be trapped around DFs for a long time. Since a DF is a localized B_z hump, electrons can leave this region along the field lines if they have a nonzero parallel velocity. Although C. Huang et al. (2015) argued that a positive electrostatic potential formed around the DF can provide a trapping mechanism, electrons with sufficient high perpendicular energy cannot be trapped. Therefore, the flux of energetic electrons with pitch angles around 90° is limited by the electron loss process, even if the DF is growing and the power of betatron acceleration is positive. For electrons with pitch angles around 0° and 180° , they are easily trapped along the closed magnetic field lines and get long-period Fermi accelerations. Therefore, the flux of energetic electrons with pitch angles around 0° and 180° is continuously increasing; at $\Omega_i t = 46$, it is comparable to those with pitch angles around 90° , forming Rolling-pin distribution; at $\Omega_i t = 52$, it exceeds those with pitch angles around 90° , forming Cigar distribution. The flux

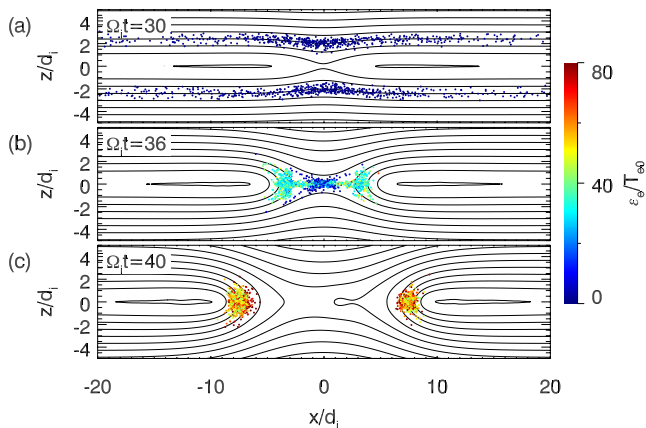


Figure 5. The spatial distributions for electrons with energy $\varepsilon > 50T_{e0}$ and pitch angle $60^\circ < \theta < 120^\circ$ from $\Omega_i t = 42$ at $\Omega_i t =$ (a) 30, (b) 36, and (c) 40, respectively. The colors represent the energies of electrons.

is shown in Figure 6. Here, f is the averaged value of f over these electrons. Panels (a–d) show the energy ε , magnetic field at the electron’s position, magnetic moment μ , and α (α is defined as $\alpha = |\theta - 90^\circ|$). Under this definition, electrons with pitch angle around 90° have $\alpha \approx 0^\circ$, electrons with pitch angles around 0° and 180° have $\alpha \approx 90^\circ$, an isotropic distribution should have $\alpha \approx 32.7^\circ$). At $\Omega_i t = 30$, these electrons have not been accelerated and have low energy. Most of these electrons are located in the lobe region around $z = \pm 2.0d_i$. Then, these electrons experience a two-step acceleration process. At around $\Omega_i t = 36$, most of the electrons are located close to the reconnection x-line as shown in Figure 5b. From Figure 6, we find that the average energy of these electrons increases quickly. In this acceleration period, the local magnetic field reaches a minimum, the magnetic moment changes greatly, and these electrons experience strong pitch-angle scattering. α decreases because the pitch angles of some electrons entering the flux pileup region are around 90° . These results indicate that these electrons experience a nonadiabatic acceleration process near the reconnection x-line. After $\Omega_i t = 36$, these electrons experience a long period and slower acceleration

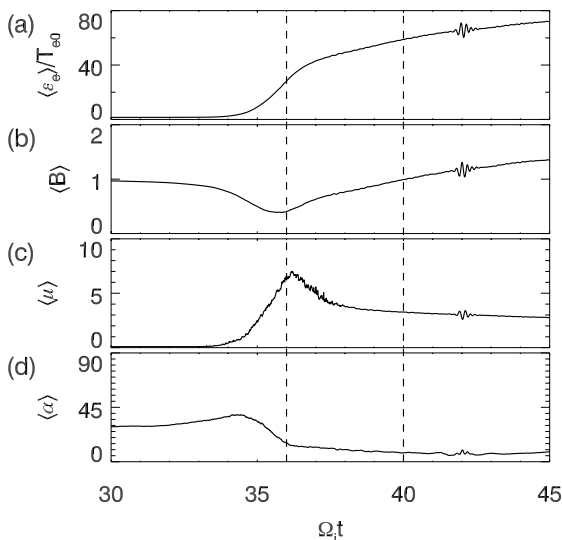


Figure 6. Time evolution of the averaged (a) energy, (b) local magnetic field, (c) magnetic moment, and (d) $\alpha = |\theta - 90^\circ|$, where θ is the pitch angle, for electrons with energy $\varepsilon > 50T_{e0}$ and pitch angle $60^\circ < \theta < 120^\circ$ from $\Omega_i t = 42$. The two vertical dashed lines denote $\Omega_i t = 36$ and 40, respectively.

stops increasing when the propagation of the DFs is blocked. For those DFs propagating for sufficient long distances, finally Cigar distributions will dominate.

3.3. The Acceleration Processes of the Energetic Electrons at the DFs

Then, we will study the detailed acceleration processes of the energetic electrons in Pancake and Cigar distributions (Rolling-pin distribution is only a transition state from Pancake to Cigar distribution). We trace the energetic electrons with energy $\varepsilon > 50T_{e0}$ and pitch angle $60^\circ < \theta < 120^\circ$ at $\Omega_i t = 42$ for Pancake distributions and energetic electrons with energy $\varepsilon > 50T_{e0}$ and pitch angle $\theta < 30^\circ$ or $> 150^\circ$ at $\Omega_i t = 52$ for Cigar distributions. The results are shown in Figures 5–8.

In Figure 5, we retrace the energetic electrons forming the Pancake distribution at $\Omega_i t = 42$ to $\Omega_i t = 30, 36$, and 40, respectively. The colors represent the electron energy and the black curves show the magnetic field lines. The detailed acceleration process of these energetic electrons is shown in Figure 6. Here, f is the averaged value of f over these electrons. Panels (a–d) show the energy ε , magnetic field at the electron’s position, magnetic moment μ , and α (α is defined as $\alpha = |\theta - 90^\circ|$). Under this definition, electrons with pitch angle around 90° have $\alpha \approx 0^\circ$, electrons with pitch angles around 0° and 180° have $\alpha \approx 90^\circ$, an isotropic distribution should have $\alpha \approx 32.7^\circ$). At $\Omega_i t = 30$, these electrons have not been accelerated and have low energy. Most of these electrons are located in the lobe region around $z = \pm 2.0d_i$. Then, these electrons experience a two-step acceleration process. At around $\Omega_i t = 36$, most of the electrons are located close to the reconnection x-line as shown in Figure 5b. From Figure 6, we find that the average energy of these electrons increases quickly. In this acceleration period, the local magnetic field reaches a minimum, the magnetic moment changes greatly, and these electrons experience strong pitch-angle scattering. α decreases because the pitch angles of some electrons entering the flux pileup region are around 90° . These results indicate that these electrons experience a nonadiabatic acceleration process near the reconnection x-line. After $\Omega_i t = 36$, these electrons experience a long period and slower acceleration than that at the x-line. During this period, the local magnetic field increases gradually, the magnetic moment is nearly constant, and the pitch angles of these electrons are close to 90° . These signatures are consistent with betatron acceleration, and it is also demonstrated in Figure 5c; these electrons are located near the DF regions. Note that Figure 5 only shows the positions of electrons, which form the Pancake distribution in the early stage; in the later stage, these electrons will gradually leave the DFs along the field lines due to the loss process described in Section 3.2.

In Figure 7, we retrace the energetic electrons forming the Cigar distribution at $\Omega_i t = 52$ to $\Omega_i t = 30, 35$, and 49, respectively. The detailed acceleration process of these energetic electrons is shown in Figure 8. Different from Figure 6c, we plot the secondary adiabatic invariant $p_{\parallel} l_s$ averaged over these electrons in Figure 8c. Here, p_{\parallel} is the electron parallel momentum, $l_s = L_x - L_{DF}$, where L_x is the length of the simulation domain and L_{DF} is the distance between the two DFs. Similar to Figure 5, these electrons are located in the lobe region initially. These electrons also show a two-step acceleration process. At around $\Omega_i t = 35$, there is a quick acceleration period similar to that in Figure 6. This acceleration period is also dominated by magnetic reconnection. In Figure 7b, except for the electrons located around the reconnection x-line, there are still a large number of electrons located in a large area near the separatrices. The reason is that these electrons move parallel or antiparallel to the magnetic field; they can spread in a long range along the field lines. After $\Omega_i t = 35$,

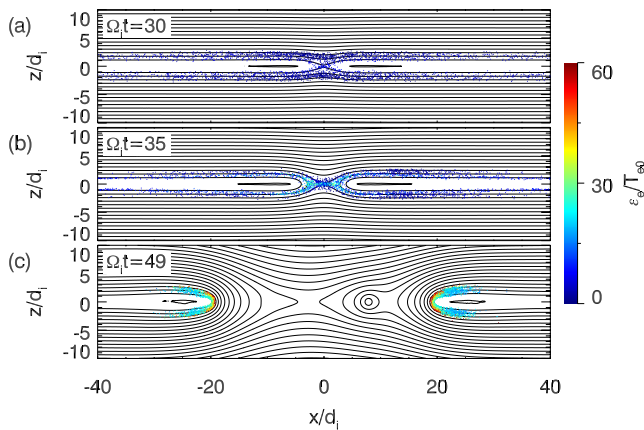


Figure 7. The spatial distributions for electrons with energy $\varepsilon > 50T_{e0}$ and pitch angle $\theta < 30^\circ$ or $> 150^\circ$ from $\Omega_i t = 52$ at $\Omega_i t =$ (a) 30, (b) 35, and (c) 49, respectively. The colors represent the energies of electrons.

these electrons experience several short-period accelerations where the energy of these electrons increases quickly. Each acceleration period corresponds to a peak in the local magnetic field. Figure 7c shows the position of these electrons at $\Omega_i t = 49$. Most of these electrons are located around the DFs. We also check other acceleration periods with peaks in magnetic field and the situations are similar (not shown). During the whole process, the secondary adiabatic invariant is nearly a constant and the pitch angles of these electrons are around 0° and 180° . These results indicate that Fermi acceleration dominates in this period.

We should note that for both groups of energetic electrons forming Pancake and Cigar distributions, magnetic reconnection plays an important role in their acceleration processes. The energy gain at the reconnection x-line is comparable to that at the DFs. Since both betatron and Fermi accelerations are sensitive to the initial energy, electrons with higher initial energy can get a more efficient acceleration. A preacceleration is necessary for the formation of both Pancake and Cigar distributions.

4. Conclusions and Discussion

In this paper, we perform a 2D PIC simulation to study the formation of Pancake, Rolling pin, and Cigar distributions of energetic electrons at DFs. The DFs in our simulation are driven by magnetic reconnection. The energetic electrons at DFs come from the lobe region and experience a two-step acceleration process. At first, they experience a nonadiabatic acceleration at the reconnection x-line. Then, electrons get further acceleration at DFs through betatron and Fermi mechanisms. The energy gain at the x-line is comparable to that at the DFs. During the propagation of DFs, these energetic electrons form Pancake, Rolling pin, and Cigar distributions in sequence. These distributions are formed in the different stages of acceleration process at DFs. In the early stage, Pancake distributions are formed through betatron acceleration. During this stage, the flux of energetic electrons with pitch angles around 0° and 180° is low because these electrons have no time to be reflected many times to get Fermi acceleration. However, the electrons with pitch angles around 90° are difficult to be trapped around the DFs for a long time, and their flux saturates quickly, while the electrons with pitch angles around 0° and 180° can be easily trapped inside the closed field lines and get continuous Fermi acceleration during the propagation of the DFs. Therefore, in the later stage, the flux of energetic electrons with pitch angles around 0° and 180° gradually increases and at last exceeds that of energetic electrons with pitch angles around 90° , forming Rolling pin and Cigar distributions in sequence.

Our results can also explain the observation in M. Y. Wu et al. (2013). The reason for the lower occurrence rate for Cigar distributions in the middle tail is that electrons have no time to be reflected many times at the DFs in the middle tail. While the reason for the increased occurrence rate for Cigar distributions in the near-Earth region is that electrons with pitch angles around 0° and 180° can be trapped along the closed field lines and get more Fermi accelerations due to the shrinking of the magnetic field lines.

We find that the power of betatron acceleration is much smaller than that of Fermi acceleration whenever the energetic electrons show Pancake, Rolling pin, or Cigar distributions. This result indicates that it should be careful to simply relate the pitch angle distributions of energetic electrons to the power of acceleration mechanisms during observations (Akhan-Tafti et al., 2019; Eriksson et al., 2020; Zhong et al., 2020). Because we can only learn the local acceleration power along the trajectory of the

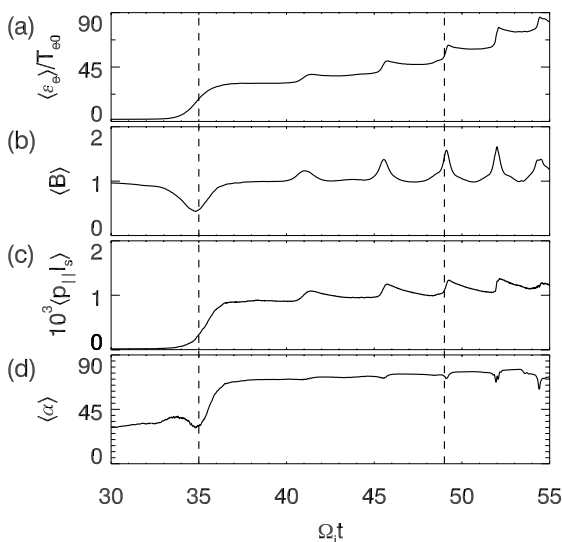


Figure 8. Time evolution of the averaged (a) energy, (b) local magnetic field, (c) secondary adiabatic invariant, and (d) $\alpha = |\theta - 90^\circ|$, where θ is the pitch angle for electrons with energy $\varepsilon > 50T_{e0}$ and pitch angle $\theta < 30^\circ$ or $> 150^\circ$ from $\Omega_i t = 52$. The two vertical dashed lines denote $\Omega_i t = 35$ and 49, respectively.

satellite, while the whole acceleration process of electrons is unknown. Especially for different acceleration mechanisms and electrons with different pitch angles, the acceleration process can be critical to determine the energy gain.

In our simulation, electrons can pass the boundaries in the x direction and get multiple Fermi accelerations by the DFs. While in the magnetotail, electrons are reflected at the mirror points near the Earth and return to the DFs to get multiple Fermi accelerations. These two processes are similar except that in the latter case, electrons with extremely small pitch angles may lose into the atmosphere. If we assume that the magnetic field at the DFs is around 10 nT, electrons that reach the region with magnetic field around 10000 nT (typical magnetic field in the auroral acceleration region) can lose into the atmosphere. Electrons with pitch angles less than 1.8° at the DFs will lose. These electrons do not significantly affect our main results.

Data Availability Statement

The simulation data set is available at <https://dx.doi.org/10.12176/01.99.01458>.

Acknowledgments

This work is supported by the NSFC grant 41774169, Key Research Program of Frontier Sciences, CAS (QYZDJ-SSW-DQC010), the Strategic Priority Research Program of Chinese Academy of Sciences, Grant No. XDB 41000000, and the Fundamental Research Funds for the Central Universities WK2080000164.

References

- Akhavan-Tafti, M., Slavin, J. A., Sun, W. J., Le, G., & Gershman, D. J. (2019). MMS observations of plasma heating associated with FTE growth. *Geophysical Research Letters*, *46*(22), 12654–12664. <https://doi.org/10.1029/2019gl084843>
- Angelopoulos, V., Baumjohann, W., Kennel, C. F., Coroniti, F. V., Kivelson, M. G., Pellat, R., et al. (1992). Bursty bulk flows in the inner central plasma sheet. *Journal of Geophysical Research*, *97*(A4), 4027–4039. <https://doi.org/10.1029/91ja02701>
- Angelopoulos, V., Kennel, C. F., Coroniti, F. V., Pellat, R., Kivelson, M. G., Walker, R. J., et al. (1994). Statistical characteristics of bursty bulk flow events. *Journal of Geophysical Research*, *99*(A11), 21257–21280. <https://doi.org/10.1029/94JA01263>
- Birn, J., & Hesse, M. (2013). The substorm current wedge in MHD simulations. *Journal of Geophysical Research: Space Physics*, *118*(6), 3364–3376. <https://doi.org/10.1002/jgra.50187>
- Birn, J., Thomsen, M. F., & Hesse, M. (2004). Electron acceleration in the dynamic magnetotail: Test particle orbits in three-dimensional magnetohydrodynamic simulation fields. *Physics of Plasmas*, *11*(5), 1825–1833. <https://doi.org/10.1063/1.1704641>
- Borovsky, J. E., Birn, J., Echim, M. M., Fujita, S., Lysak, R. L., Knudsen, D. J., et al. (2019). Quiescent discrete auroral arcs: A review of magnetospheric generator mechanisms. *Space Science Reviews*, *216*(1), 1–39. <https://doi.org/10.1007/s11214-019-0619-5>
- Buchner, J., & Zelenyi, L. M. (1989). Regular and chaotic charged-particle motion in magnetotail-like field reversals 1. Basic theory of trapped motion. *Journal of Geophysical Research*, *94*(A9), 11821–11842. <https://doi.org/10.1029/JA094iA09p11821>
- Cao, J. B., Ma, Y. D., Parks, G., Reme, H., Dandouras, I., Nakamura, R., et al. (2006). Joint observations by Cluster satellites of bursty bulk flows in the magnetotail. *Journal of Geophysical Research*, *111*(A4), A04206. <https://doi.org/10.1029/2005ja011322>
- Chang, C., Huang, K., Lu, Q. M., Sang, L. L., Lu, S., Wang, R. S., et al. (2021). Particle-in-cell simulations of electrostatic solitary waves in asymmetric magnetic reconnection. *Journal of Geophysical Research: Space Physics*, *126*(7), e2021JA029290. <https://doi.org/10.1029/2021JA029290>
- Dahlin, J. T., Drake, J. F., & Swisdak, M. (2014). The mechanisms of electron heating and acceleration during magnetic reconnection. *Physics of Plasmas*, *21*(9), 092304. <https://doi.org/10.1063/1.4894484>
- Deng, X. H., Ashour-Abdalla, M., Zhou, M., Walker, R., El-Alaoui, M., Angelopoulos, V., et al. (2010). Wave and particle characteristics of earthward electron injections associated with dipolarization fronts. *Journal of Geophysical Research*, *115*, A09225. <https://doi.org/10.1029/2009ja015107>
- Drake, J. F., Swisdak, M., Che, H., & Shay, M. A. (2006). Electron acceleration from contracting magnetic islands during reconnection. *Nature*, *443*(7111), 553–556. <https://doi.org/10.1038/nature05116>
- Eriksson, E., Vaivads, A., Alm, L., Graham, D. B., Khotyaintsev, Y. V., & Andre, M. (2020). Electron acceleration in a magnetotail reconnection outflow region using magnetospheric multiscale data. *Geophysical Research Letters*, *47*(1), e2019GL085080. <https://doi.org/10.1029/2019GL085080>
- Fu, H., Grigorenko, E. E., Gabrielse, C., Liu, C., Lu, S., Hwang, K. J., et al. (2019). Magnetotail dipolarization fronts and particle acceleration: A review. *Science China Earth Sciences*, *63*(2), 235–256. <https://doi.org/10.1007/s11430-019-9551-y>
- Fu, H. S., Khotyaintsev, Y. V., Andre, M., & Vaivads, A. (2011). Fermi and betatron acceleration of suprathermal electrons behind dipolarization fronts. *Geophysical Research Letters*, *38*, L16104. <https://doi.org/10.1029/2011GL048528>
- Fu, H. S., Khotyaintsev, Y. V., Vaivads, A., André, M., Sergeev, V. A., Huang, S. Y., et al. (2012). Pitch angle distribution of suprathermal electrons behind dipolarization fronts: A statistical overview. *Journal of Geophysical Research*, *117*(A12), A12221. <https://doi.org/10.1029/2012ja018141>
- Fu, X. R., Lu, Q. M., & Wang, S. (2006). The process of electron acceleration during collisionless magnetic reconnection. *Physics of Plasmas*, *13*(1), 423–430. <https://doi.org/10.1063/1.2164808>
- Huang, C., Lu, Q. M., & Wang, S. (2010). The mechanisms of electron acceleration in antiparallel and guide field magnetic reconnection. *Physics of Plasmas*, *17*(7), 072306. <https://doi.org/10.1063/1.3457930>
- Huang, C., Wu, M. Y., Lu, Q. M., Wang, R. S., & Wang, S. (2015). Electron acceleration in the dipolarization front driven by magnetic reconnection. *Journal of Geophysical Research: Space Physics*, *120*(3), 1759–1765. <https://doi.org/10.1002/2014JA020918>
- Huang, K., Lu, Q. M., Wang, R. S., & Wang, S. (2020). Spontaneous growth of the reconnection electric field during magnetic reconnection with a guide field: A theoretical model and particle-in-cell simulations. *Chinese Physics B*, *29*(7), 075202. <https://doi.org/10.1088/1674-1056/ab8da0>
- Khotyaintsev, Y. V., Cully, C. M., Vaivads, A., Andre, M., & Owen, C. J. (2011). Plasma jet braking: Energy dissipation and nonadiabatic electrons. *Physical Review Letters*, *106*(16), 165001. <https://doi.org/10.1103/PhysRevLett.106.165001>

- Li, X., Guo, F., Li, H., & Li, G. (2017). Particle acceleration during magnetic reconnection in a low-beta plasma. *The Astrophysical Journal*, 843(1), 21. <https://doi.org/10.3847/1538-4357/aa745e>
- Liu, C. M., Fu, H. S., Xu, Y., Cao, J. B., & Liu, W. L. (2017). Explaining the rolling-pin distribution of suprathermal electrons behind dipolarization fronts. *Geophysical Research Letters*, 44(13), 6492–6499. <https://doi.org/10.1002/2017GL074029>
- Lu, Q., Huang, C., Xie, J., Wang, R., Wu, M., Vaivads, A., & Wang, S. (2010). Features of separatrix regions in magnetic reconnection: Comparison of 2-D particle-in-cell simulations and Cluster observations. *Journal of Geophysical Research*, 115(A11), A11208. <https://doi.org/10.1029/2010ja015713>
- Lu, Q., Wang, H., Huang, K., Wang, R., & Wang, S. (2018). Formation of power law spectra of energetic electrons during multiple X line magnetic reconnection with a guide field. *Physics of Plasmas*, 25(7), 072126. <https://doi.org/10.1063/1.5034012>
- Lu, S., Angelopoulos, V., & Fu, H. S. (2016). Suprathermal particle energization in dipolarization fronts: Particle-in-cell simulations. *Journal of Geophysical Research: Space Physics*, 121(10), 9483–9500. <https://doi.org/10.1002/2016ja022815>
- Lu, S., Lu, Q., Lin, Y., Wang, X., Ge, Y., Wang, R., et al. (2015). Dipolarization fronts as earthward propagating flux ropes: A three-dimensional global hybrid simulation. *Journal of Geophysical Research: Space Physics*, 120(8), 6286–6300. <https://doi.org/10.1002/2015ja021213>
- Nakamura, R., Baumjohann, W., Klecker, B., Bogdanova, Y., Balogh, A., Rème, H., et al. (2002). Motion of the dipolarization front during a flow burst event observed by Cluster. *Geophysical Research Letters*, 29(20). <https://doi.org/10.1029/2002GL015763>
- Nakamura, R., Baumjohann, W., Panov, E., Petrukovich, A. A., Angelopoulos, V., Volwerk, M., et al. (2011). Flux transport, dipolarization, and current sheet evolution during a double-onset substorm. *Journal of Geophysical Research*, 116, A00i36. <https://doi.org/10.1029/2010ja015865>
- Nakamura, R., Retino, A., Baumjohann, W., Volwerk, M., Erkaev, N., Klecker, B., et al. (2009). Evolution of dipolarization in the near-Earth current sheet induced by Earthward rapid flux transport. *Annales Geophysicae*, 27(4), 1743–1754. <https://doi.org/10.5194/angeo-27-1743-2009>
- Northrop, T. G. (1963). Adiabatic charged-particle motion. *Reviews of Geophysics*, 1(3), 283–304. <https://doi.org/10.1029/RG001i003p00283>
- Ohtani, S., Shay, M. A., & Mukai, T. (2004). Temporal structure of the fast convective flow in the plasma sheet: Comparison between observations and two-fluid simulations. *Journal of Geophysical Research*, 109(A3), A03210. <https://doi.org/10.1029/2003ja010002>
- Runov, A., Angelopoulos, V., Sitnov, M. I., Sergeev, V. A., Bonnell, J., McFadden, J. P., et al. (2009). THEMIS observations of an earthward-propagating dipolarization front. *Geophysical Research Letters*, 36, L14106. <https://doi.org/10.1029/2009GL038980>
- Runov, A., Angelopoulos, V., & Zhou, X. Z. (2012). Multipoint observations of dipolarization front formation by magnetotail reconnection. *Journal of Geophysical Research*, 117, A05230. <https://doi.org/10.1029/2011JA017361>
- Sitnov, M. I., Buzulukova, N., Swisdak, M., Merkin, V. G., & Moore, T. E. (2013). Spontaneous formation of dipolarization fronts and reconnection onset in the magnetotail. *Geophysical Research Letters*, 40(1), 22–27. <https://doi.org/10.1029/2012GL054701>
- Sitnov, M. I., Swisdak, M., & Divin, A. V. (2009). Dipolarization fronts as a signature of transient reconnection in the magnetotail. *Journal of Geophysical Research*, 114, A04202. <https://doi.org/10.1029/2008JA013980>
- Volwerk, M., Lui, A. T. Y., Lester, M., Walsh, A. P., Alexeev, I., Cao, X., et al. (2008). Magnetotail dipolarization and associated current systems observed by Cluster and Double Star. *Journal of Geophysical Research*, 113(A8), A08S90. <https://doi.org/10.1029/2007ja012729>
- Wang, H. Y., Lu, Q. M., Huang, C., & Wang, S. (2016). The mechanisms of electron acceleration during multiple X line magnetic reconnection with a guide field. *The Astrophysical Journal*, 821(2), 84. <https://doi.org/10.3847/0004-637x/821/2/84>
- Wu, M., Huang, C., Lu, Q., Volwerk, M., Nakamura, R., Vörös, Z., et al. (2015). In situ observations of multistage electron acceleration driven by magnetic reconnection. *Journal of Geophysical Research: Space Physics*, 120(8), 6320–6331. <https://doi.org/10.1002/2015ja021165>
- Wu, M. Y., Lu, Q., Volwerk, M., Voros, Z., Zhang, T. L., Shan, L. C., & Huang, C. (2013). A statistical study of electron acceleration behind the dipolarization fronts in the magnetotail. *Journal of Geophysical Research: Space Physics*, 118(8), 4804–4810. <https://doi.org/10.1002/jgra.50456>
- Wu, P., Fritz, T. A., Larvaud, B., & Lucek, E. (2006). Substorm associated magnetotail energetic electrons pitch angle evolutions and flow reversals: Cluster observation. *Geophysical Research Letters*, 33(17), 123–154. <https://doi.org/10.1029/2006GL028297>
- Zhang, H., Pu, Z. Y., Cao, X., Fu, S. Y., Liu, Z. X., Ma, Z. W., et al. (2007). TC-1 observations of flux pileup and dipolarization-associated expansion in the near-Earth magnetotail during substorms. *Geophysical Research Letters*, 34(3), L03104. <https://doi.org/10.1029/2006gl028326>
- Zhong, Z. H., Zhou, M., Tang, R. X., Deng, X. H., Turner, D. L., Cohen, I. J., et al. (2020). Direct evidence for electron acceleration within ion-scale flux rope. *Geophysical Research Letters*, 47(1), e2019GL085141. <https://doi.org/10.1029/2019GL085141>
- Zhou, X. Z., Angelopoulos, V., Sergeev, V. A., & Runov, A. (2010). Accelerated ions ahead of earthward propagating dipolarization fronts. *Journal of Geophysical Research*, 115, A00i03. <https://doi.org/10.1029/2010ja015481>